Supporting Information for

Interactions between O_3 and $PM_{2.5}$ promote a regional double-high pollution event in the Yangtze River Delta, China

Xiaodong Xie[1], Yang Qin[2], Hongli Wang[3], Momei Qin[1], Yuanhang Zhang[4], Jianlin Hu[1,*]

[1] Jiangsu Key Laboratory of Intelligent Atmospheric Environment Monitoring and Carbon-Pollution Co-control, Collaborative Innovation Center of Atmospheric Environment and Equipment Technology, School of Environmental Science and Engineering, Nanjing University of Information Science and Technology, Nanjing 210044, China

[2] Henan Key Laboratory of Agrometeorological Support and Applied Technique, CMA, Henan Meteorological Observatory, Zhengzhou 450003, China

[3] State Environmental Protection Key Laboratory of Formation and Prevention of Urban Air Pollution Complex, Shanghai Academy of Environmental Sciences, Shanghai 200233, China

[4] State Key Joint Laboratory of Environmental Simulation and Pollution Control, College of Environmental Sciences and Engineering, Peking University, Beijing 100871, China

*Corresponding author:

Dr. Jianlin Hu, Email: jianlinhu@nuist.edu.cn

Contents of this file

Text S1–S7

Tables S1–S5

Figures S1–S19

S1 Modeling description

The Community Multiscale Air Quality modeling System (CMAQ) is mostly used to study $PM_{2.5}$ pollution in winter and O_3 pollution in summer.[1-3] The commonly used CMAQ is one-way coupled, using offline meteorological input to drive atmospheric chemistry, which cannot reflect the feedback of air pollution on meteorology. However, in the real atmosphere, chemistry and meteorology are mutually influential.[4] Meteorological conditions, such as solar radiation, temperature, wind speed, relative humidity (RH), and cloud cover, can influence the formation of $PM_{2.5}$ and O_3. In addition, aerosol also can directly or indirectly affect meteorology and even climate.[5, 6] Aerosol radiation transfer budget by scattering and absorbing solar radiation, by serving as the cloud condensation nuclei (CCN) to alter or affect cloud lifetime and optical properties, by heating the atmosphere to modify cloud formation, which is termed as the aerosol direct radiative effect, indirect effect, and semi-direct effect, respectively.[7-9] Owning to the dramatic development in computer power, the two-way coupled WRF-CMAQ has been taking into account the aerosol feedback mechanism, which coupled meteorological and chemical transport model. Detailed information on the two-way coupled WRF-CMAQ is described by Wong et al.[10] In the online model, both the impact of meteorology on air quality and the feedback of aerosol on meteorology are simulated. This coupled model has also been used in several types of research to investigate the direct or indirect effects of aerosol radiative on climate and air quality. [5, 11-13]

S2 Modeling configuration and emission input

The initial and boundary of meteorological inputs for WRF were derived from the National Centers for Environmental Prediction (NCEP) Final Analysis (FNL) reanalysis data, which has spatial and temporal resolutions of 0.25° and 6 h respectively. The physics options of WRF model configuration included the single-moment 6-class scheme (WSM6) microphysics scheme,[14] the Kain-Fritsch scheme for the cumulus,[15] the Pleim-Xiu land surface model for the land surface,[16] the Asymmetric Convection Model version 2 (ACM2) scheme for the planetary boundary layer (PBL),[17] and the Rapid Radiative Transfer Model for General Circulation Models (RRTMG) for the longwave and shortwave radiation.[18] The CMAQ model was configured using the SAPRC07tic gas-phase chemical mechanism and the AERO6i aerosol module. The vertical layers consisted of 43 sigma-pressure layers from the surface to 100hPa. The initial and boundary conditions of the d01 simulations were derived from the default CMAQ model. The initial and boundary conditions of the d02 were derived from the d01.

The anthropogenic emissions inventory used in this study consisted of the following three parts: 1) emissions in the YRD region (including Anhui, Jiangsu, and Zhejiang provinces as well as Shanghai municipality), which were provided by the Shanghai Academy of Environmental Sciences with a 4 km grid

resolution with 198×228 grids for the year 2019;[19] 2) emission in other areas of mainland China, which were extracted from the Multi-resolution Emission Inventory for China (http://meicmodel.org/) of 2017 with a 0.25° × 0.25° horizontal grid resolution; 3) emissions in other countries and regions in Asia, which were generated from the gridded 0.25°× 0.25°resolution Regional Emission inventory in Asia version 3.2 (REASv3.2).[20] The Model of Emissions of Gases and Aerosols from Nature version 2.1 (MEGAN2.1) was used to generate the emissions from natural sources.[21] Most details about the processing procedure for biogenic emissions can be found in Qiao, et al.[22]. The Fire Inventory from NCAR (FINN) provided open biomass burning emissions, which are based on satellite observations.[23]

S3 Observation data

Water-soluble ions were measured by the Gas Components and Aerosol Monitoring systems (MARGA 1S). OC and EC were analyzed by the thermal/optical transmittance methods (Sunset Lab). The detection limits of water-soluble ions are 0.10 μg/m^3 for Na^+, 0.08 μg/m^3 for Ca^{2+}, 0.05 μg/m^3 for NO_3^-, 0.08 μg/m^3 for SO_4^{2-}, and 0.08 μg/m^3 for NH_4^+, respectively. Meanwhile, the detection limits of OC and EC are 0.32 and 0.004 μg/m^3, respectively. Detailed descriptions of the instrumentation can be found in other studies (Xu et al., 2018; Zhang et al., 2020). The monitoring site in Nanjing is at Caochangmen (32°3′ N, 118.44′ E) and the monitoring site in Shanghai is at the Shanghai monitoring station (31°45′ N, 121.59′ E), both of which are surrounded by residential areas.

S4 Model Evaluation

A reasonable prediction of meteorological conditions is essential for simulating air pollutions.[24] The meteorological parameters were validated by comparing the model results with hourly surface observations of 2m air temperature (T2) and relative humidity (RH), 10-m wind direction (WD) and wind speed (WS). Figure S3 shows the comparison between the simulated and observed meteorological conditions for the eight cities in the YRD region affected by DHP. The model could accurately simulate the trend of meteorological conditions in these eight cities. Model performance statistical metrics of mean bias (MB), mean error (ME), and root mean square error (RMSE) based on simulated and observed meteorological variables are given in Table S1. The table also shows the benchmarks proposed by Emery and Tai [25]. Although T2 is slightly underestimated and the MB is slightly larger than the benchmarks, the ME for T2 and other statistical metrics of the meteorological variables are with in the given benchmarks. Therefore, the model showed a reasonable model performance.

Figure S4 depicts the times series comparing simulated and observed $PM_{2.5}$ and O_3 concentrations in the

cities. The statistical verification of the simulated surface $PM_{2.5}$ and O_3 concentrations are shown in Table S2 with the normalized mean bias (NMB), normalized mean error (NME), correlation coefficient (R), and index of agreement (IOA). The concentrations of $PM_{2.5}$ and O_3 are slightly overestimated. However, the R and IOA are relatively well, with values of 0.87 and 0.91 for $PM_{2.5}$, and 0.91 and 0.94 for O_3, respectively, while other statistical indicators are within the model performance benchmarks suggested by Emery et al.[26] The high-values areas of the regional DHP day are in good agreement with the observed values (Figure S5), showing a good simulation ability of the model for the regional DHP days. Figure S6 and Figure S7 present the temporal variations of the simulated and measured gaseous pollutants (SO_2 and NO_2) and the major components of $PM_{2.5}$ in Shanghai and Nanjing. Generally, secondary inorganic ions, especially nitrate, are well simulated in both cities with correlation coefficients of 0.85 and 0.71, respectively. All of these suggest that the coupled WRF-CMAQ model have a better ability to simulate pollutants.

In conclusion, despite some deviations, the simulated meteorology and chemical fields show good agreement with observations, which provides a solid foundation for utilizing the simulation results to analyze the DHP event.

S5 $PM_{2.5}$ and O_3 transport

Figure S8 and Figure S9 show the spatial distribution of near-surface $PM_{2.5}$ and O_3 concentrations overlaid with wind fields during the entire regional DHP process on 5–9 April, from the pollution formation to the removal, respectively. According to the spatial distribution, the DHP was caused by local generation and local regional transportation. From 5 to 6 April, $PM_{2.5}$ (Figure S8a-c) and O_3 (Figure S9a-c) began to accumulate in the northern Jiangsu and coastal areas in the eastern part of the YRD region. Starting in the afternoon of 7 April, the northerly wind transported $PM_{2.5}$ (Figure S8e) and O_3 (Figure S9e) to central Jiangsu and the vicinity of the Yangtze River Estuary. At 03:00 on 8 April (Figure S8f), the surface $PM_{2.5}$ was transported from the upstream direction of Shanghai towards the downstream direction of Nanjing under the prevailing easterly winds. Similar to $PM_{2.5}$, there was also a very significant upstream and downstream transport of near-surface O_3 at 14:00 on 8 April (Figure S9f). Thus, from the evening of 7 April to the noon of 8 April, the strong $PM_{2.5}$ and O_3 transport in the direction of Shanghai to Nanjing would have an impact on the DHP in the five cities of Shanghai, Suzhou, Changzhou, Nanjing, and Chuzhou on this transport pathway. It also affected Hangzhou and Shaoxing near Shanghai simultaneously. By 9 April, under the strong northerly winds, $PM_{2.5}$ (Figure S8h) and O_3 (Figure S9h) pollution in the YRD region dissipated.

Eastern China is vulnerable to dust from the northwest in spring [27, 28]. Wang, et al. [29] found that the aerosol radiation interaction caused by a strong dust process in the YRD could increase the concentration of O_3 and secondary inorganic aerosols. However, the mean value of Ca^+ concentration at the Nanjing site during the

observation period was 0.41 μg/m^3 and the maximum value was 0.9 μg/m3 (Figure S10), which was much smaller than the maximum Ca^+ concentration (~12μg/m^3) measured by Wang et al in 2019 when Nanjing was affected by dust. Therefore, here we excluded the influence of dust during the simulation period.

In order to analyze the formation and evolution of O_3 and $PM_{2.5}$ along the transport path during the DHP in the YRD, based on the model results, the average concentrations of $PM_{2.5}$ and O_3 along the regional transport path from Shanghai to Nanjing (Figure S1b, the red line), and the boundary layer height during the period of 5–8 April were selected to study the vertical distribution of $PM_{2.5}$ and O_3 as well as atmospheric boundary layer vertical structure (Figure S11). Compared with 5–6 April, $PM_{2.5}$ pollution was mainly concentrated during the evening of 7 April to the morning of 8 April, and higher concentrations of $PM_{2.5}$ were observed from surface to 0.6km above ground (Figure S11a). O_3 concentration near the surface decreases rapidly after sunset due to the depletion of O_3 dry deposition and NO titration, while O_3 concentrations at high altitude remains relatively due to the lack of O_3 depletion. Therefore, low O_3 in the stable boundary layer and high O_3 in the residual layer can be observed (Figure S11b). It was worth noting that higher concentrations of O_3 were present in the atmospheric residual layer at about 0.3–1.0 km on the nighttime of 7 April compared to the previous two nighttime. Both the vertical distribution of $PM_{2.5}$ and O_3 concentrations dropped rapidly after 00:00 on 8 April, especially for O_3.

To further study the transmission process of DHP in the YRD, Figure S12 shows the vertical profile of the $PM_{2.5}$ and O_3 superimposed by wind field along the regional transport pathway (Figure S1b, the black line) from the afternoon of 7 April to the morning of 8 April. The vertical distribution of $PM_{2.5}$ and O_3 are both controlled by the diurnal changes of the atmospheric boundary layer. During the daytime, strong turbulent mixing brought $PM_{2.5}$ (Figure S12a) and O_3 (Figure S12f) to high altitudes, which was conducive to the vertical diffusion of $PM_{2.5}$ and O_3. After sunset, due to the radiation cooling near the ground, a stable boundary layer was formed rapidly, which suppressed the vertical diffusion of $PM_{2.5}$ and O_3. Meanwhile, $PM_{2.5}$ accumulated within the boundary layer (Figure S12b), while a high concentration of O_3 was maintained at a high altitude owing to the sharp depletion of O_3 concentration near the ground (Figure S12g). Figure S13 shows the synoptic situation of the sea level pressure (SLP) and the geopotential height of 850hPa at night on 7 April, respectively. The YRD region (the black box) was under the influenc of southwest low pressure near the surface, and the dominat wind direction was easterly (Figure S13a). While the dominat wind direction was westerly at 850hPa(about 1.5km) under the influence of high pressure (Figure S13b). Figure S12 also presents the opposite wind field in the upper and lower layers during this period. The westerly wind prevailed in the upper layer (above about 1.5km), while the easterly wind prevailed in the lower layer (below about 0.6km), especially near the ground. Under the effect of the prevailing easterly winds near the surface, high $PM_{2.5}$ concentrations in the eastern YRD were continuously transported from Shanghai direction to Nanjing (Figure

S12b-d). The surface transport of O_3 was not obvious in Figure S12g-h because of the large consumption of O_3 near the ground at nighttime. However, we could see from Figure 1 that O_3 concentration in the downwind area in Nanjing increased by 20 $\mu g/m^3$ in the early morning of 8 April. Simultaneously, the PA results also displayed that the O_3 in Nanjing was significantly affected by horizontal transport at 00-07 on 8 April (Figure S15), which indicated that there was O_3 transport from upwind (Shanghai) to downwind (Nanjing) at night despite a large amount of O_3 consumption near the ground at night. Same as the results in Figure S11, the vertical profile distribution of $PM_{2.5}$ and O_3 concentrations have decreased significantly on the evening of 7 April (Figure S12b-d and Figure S12g-h). In particular, the vertical distribution of O_3 showed that the vertical distribution of O_3 concentration in the downstream area was low, while the vertical distribution of O_3 concentration in the upstream close to the source area (Shanghai eastern coastal area) was high. After sunrise on 8 April, strong vertical mixing made the convective boundary layer develop vigorously, which was conducive to the vertical diffusion of $PM_{2.5}$ and reduced the $PM_{2.5}$ concentration near the surface (Figure S12e). Meanwhile, the development of the troposphere also broke the maintenance of high O_3 in the residual layer, and the development of surface turbulence transports a high concentration of O_3 in the residual layer to the ground, which could contribute to the high surface O_3 concentrations in the morning (Figure. S12J).

Figure S14 presents the spatial distribution of O_3 concentration and wind vector field at the surface, 500m, and 900m on 8 April at 00,02,05, and 07 hours. It can be clearly seen from Figure S14 that wind direction at the surface, 500m, and 900m was obviously inconsistent. In the direction of the regional transport path, the average wind directions of the surface, 500 m, and 900 m at 00-07 on 8 April were 90.2, 143.9, and 173.1(°), respectively. The prevailing wind direction changed from easterly to southerly as the height rising. The O_3 in the residual layer gradually shifted from westerly to northerly transport along the regional transport path near the ground as the height rose, which led to a gradually decreasing in O_3 concentration above the residual layer along the regional transport path as the height rose, and gradually decreasing in O_3 concentrations along the regional transport path as it transported to downwind. Therefore, the vertical distribution of O_3 decreased significantly with time in the residual layer along the transport path, and the decrease was more pronounced in the downstream area (Nanjing area) than in the upstream area. Overall, with the passing time, the O_3 concentration in the residual layer on the regional transport path decreased gradually.

Hu, et al. [30] found that high O_3 concentrations in the nighttime residual layer are transported from upwind areas to downwind areas by the prevailing winds, and the high O_3 concentrations are entrained to the ground through vertical mixing in the downwind areas in the next morning, contributing significantly to the elevated O_3 concentrations in the downing areas on the next day. Figure S15 demonstrates that the hourly contribution of vertical mixing and photochemical reactions to O_3 within boundary layer along the regional transport pathway from Shanghai to Nanjing during the daytime on 5–8 April. In contrast to Hu et al, we found that

although there was upwind-to-downwind transport in the residual layer during the nighttime of 7 April, the O_3 concentration in the residual layer along the transport pathway decreased owing to the change of the upper-air wind direction(Figure S14). The hourly average vertical mixing contributions of O_3 in the boundary layer along the Shanghai-Nanjing transport pathway were 24.4, 23.3, 25.9, and 21.5 μg/m^3 during the morning of 5–8 April, when vertical mixing was strong from 08-10 a.m. (Figure S15). In the morning of 5-8 April in Nanjing (08-10:00), the hourly average vertical mixing contributions of O_3 in the boundary layer were 24.0, 20.18, 22.1, and 17.3 μg/m3 (Figure S16d), respectively. This indicated that in the downwind areas of Shanghai, the vertical mixing of O_3 on the morning of 8 April was weaker than on previous days. The total positive contribution of the photochemical reaction in the boundary layer during the daytime on 8 April along the Shanghai-Nanjing transport pathway reached 168.3μg/m^3, far exceeding that on 5–7 April (97.8， 93.1 and 103μg/m^3) (Figure S15b). The total positive contributions of photochemical reactions in the boundary layer in Nanjing on 8 April were 187.8 μg/m^3, which was also far ahead of the previous three days (71.8, 77.4, and 99.6 μg/m^3). Therefore, the strong photochemical reaction on 8 April was the main cause of ozone production in the downwind area.

S6 IPR of $PM_{2.5}$ and O_3 in Shanghai and Nanjing on 5-8 April

Figure S16 shows the IPR process of $PM_{2.5}$ and O_3 within the boundary layer of Shanghai and Nanjing administrative areas from 5–8 April. The vertical advection contribution of O_3 was generally not large,[12, 31] and the contribution in this study was also small. Therefore, we focus on the vertical mixing process in the vertical direction in this subsection. The daytime O_3 in Shanghai and Nanjing within the PBL was mainly from vertical mixing (VMIX) and chemical process (CHEM). Nocturnal chemical consumption and deposition processes (DDEP) were the main sinks of O_3. The CHEM was significantly stronger in Shanghai than that in Nanjing from 5–7 April (Figure S16). The O_3 in the early morning of 8 April was mainly from transport in Shanghai, which made the O_3 accumulate in the latter half of the night (Figure S16c). However, the local photochemistry process was relatively weaker in Shanghai during the daytime on 8 April as the daytime temperature (26.7℃) in Shanghai was lower than the previous day (30.2℃) due to the influence of cold air from the sea. Regional transport also contributed positively to O_3 in Nanjing in the early morning of 8 April. At 07:00-08:00 in the early morning, there was a relatively obvious vertical transportation. Meanwhile, the temperature in Nanjing also reached its highest during the daytime on 8 April, and Nanjing's daytime O_3 mainly came from local photochemical production. For $PM_{2.5}$, aerosol process (AERO), horizontal transport (HTRA) and vertical transport (VTRA) processes were the main sources in Shanghai and Nanjing (Figure S16a-b). The AEROs in the two cities were mainly concentrated at night, and the aerosol process in Shanghai during 5–8 April was much higher than that in Nanjing. Wang et al[32] and Zhao et al[33] found that strong

atmospheric photochemical reactions enhanced secondary aerosol formation and led to the occurrence of high concentrations of $PM_{2.5}$ and O_3. The aerosol production during the night on 7 April in Shanghai was slightly lower than that during the nighttime on 5–6 April. Whereas, during 17–21:00 on 7 April, the rapid growth of $PM_{2.5}$ was mainly affected by horizontal transportation.

S7 Influence of aerosol direct radiation effect on 5–8 April

We investigated the aerosol direct radiative effect (ADRE) on the polluted days (5–8 April). Figure S18a-d show the spatial distribution of ADRE on meteorological conditions such as shortwave radiation, PBL, temperature, and wind speed. Consistent with previous studies,[34-36] ADRE reduced the total amount of shortwave radiation reaching the surface by absorbing and scattering (Figure S18a), This leads to an overall surface cooling (Figure S18c), diminishing surface sensible heat flux, weakening vertical convection, reducing boundary layer height (Figure S18b), increasing atmospheric stability, and further reducing wind speed (Figure S18d). The ADRE caused the shortwave radiation, boundary layer height, temperature, and wind speed in the YRD region to change by about -27.6 W/m^2, -55.7 m, -0.9 °C, and -0.1 m/s on the polluted days, respectively. Ding, et al. [37] found that absorbing aerosols (such as black carbon) in the upper layer of the boundary layer heat the atmosphere, enhancing the intensity of inversion, and inhibiting the development of the boundary layer. This is noticed as the dome effect and further increases atmospheric stability.

Figure S18e-g presents the effects of ADRE on $PM_{2.5}$, nitrate, and O_3. As the major component of $PM_{2.5}$, the impacts of ADRE on nitrate are similar to that of $PM_{2.5}$. The difference between the underlying surface of land and ocean made the impact of ADRE on $PM_{2.5}$, nitrate, and O_3 different from that on land.[38] The decrease in PBL height and wind speed over land makes the atmospheric diffusion conditions stable, which aggravates the concentrations of nitrate and $PM_{2.5}$ (Figure S18e-f). Reduction in surface temperature and increasing in surface $PM_{2.5}$ concentrations weaken the photochemical reaction, which eventually leads to decreasing in O_3 concentrations (Figure S18g). Therefore, ADRE increased $PM_{2.5}$ and nitrate concentrations in the YRD region by about 2.9 and 1.5 $\mu g/m^3$, and O_3 concentrations was decreased by about 1.1 $\mu g/m^3$ on this polluted day.

References

1. Hu, J.; Chen, J.; Ying, Q.; Zhang, H., One-year simulation of ozone and particulate matter in China using WRF/CMAQ modeling system. *Atmospheric Chemistry and Physics* **2016,** *16*, (16), 10333-10350.
2. Li, L.; Xie, F.; Li, J.; Gong, K.; Xie, X.; Qin, Y.; Qin, M.; Hu, J., Diagnostic analysis of regional ozone pollution in Yangtze River Delta, China: A case study in summer 2020. *The Science of the total environment* **2021**, 151511.
3. Wang, X.; Li, L.; Gong, K.; Mao, J.; Hu, J.; Li, J.; Liu, Z.; Liao, H.; Qiu, W.; Yu, Y.; Dong, H.; Guo, S.; Hu, M.; Zeng, L.; Zhang, Y., Modelling air quality during the EXPLORE-YRD campaign – Part I. Model performance evaluation and impacts of meteorological inputs and grid resolutions. *Atmospheric Environment* **2021,** *246*, 118131.
4. Grell, G.; Baklanov, A., Integrated modeling for forecasting weather and air quality: A call for fully coupled approaches.

Atmospheric Environment **2011,** *45*, (38), 6845-6851.
5. Hong, C.; Zhang, Q.; Zhang, Y.; Davis, S. J.; Zhang, X.; Tong, D.; Guan, D.; Liu, Z.; He, K., Weakening aerosol direct radiative effects mitigate climate penalty on Chinese air quality. *Nature Climate Change* **2020,** *10*, (9), 845-850.
6. Li, J.; Han, Z.; Wu, Y.; Xiong, Z.; Xia, X.; Li, J.; Liang, L.; Zhang, R., Aerosol radiative effects and feedbacks on boundary layer meteorology and PM_{2.5} chemical components during winter haze events over the Beijing-Tianjin-Hebei region. *Atmospheric Chemistry and Physics* **2020,** *20*, (14), 8659-8690.
7. Twomey, S., Pollution and the planetary albedo. *Atmospheric Environment (1967)* **1974,** *8*, (12), 1251-1256.
8. Albrecht, B. A., Aerosols, Cloud Microphysics, and Fractional Cloudiness. *Science* **1989,** *245*, (4923), 1227-1230.
9. Ramanathan, V.; Crutzen, P. J.; Kiehl, J. T.; Rosenfeld, D., Aerosols, climate, and the hydrological cycle. *Science* **2001,** *294*, (5549), 2119-24.
10. Wong, D. C.; Pleim, J.; Mathur, R.; Binkowski, F.; Otte, T.; Gilliam, R.; Pouliot, G.; Xiu, A.; Young, J. O.; Kang, D., WRF-CMAQ two-way coupled system with aerosol feedback: software development and preliminary results. *Geoscientific Model Development* **2012,** *5*, (2), 299-312.
11. Yu, S.; Mathur, R.; Pleim, J.; Wong, D.; Gilliam, R.; Alapaty, K.; Zhao, C.; Liu, X., Aerosol indirect effect on the grid-scale clouds in the two-way coupled WRF–CMAQ: model description, development, evaluation and regional analysis. *Atmospheric Chemistry and Physics* **2014,** *14*, (20), 11247-11285.
12. Xing, J.; Wang, J.; Mathur, R.; Wang, S.; Sarwar, G.; Pleim, J.; Hogrefe, C.; Zhang, Y.; Jiang, J.; Wong, D. C.; Hao, J., Impacts of aerosol direct effects on tropospheric ozone through changes in atmospheric dynamics and photolysis rates. *Atmos Chem Phys* **2017,** *17*, (16), 9869-9883.
13. Jung, J.; Choi, Y.; Wong, D. C.; Nelson, D.; Lee, S., Role of sea fog over the Yellow Sea on air quality with the direct effect of aerosols. *Journal of geophysical research. Atmospheres : JGR* **2021,** *126*, (5).
14. Hong, S.-Y.; Kim, J.-H.; Lim, J.-o.; Dudhia, J., The WRF single moment microphysics scheme (WSM). *Journal of the Korean Meteorological Society* **2006,** *42*, 129-151.
15. Kain, J. S., The Kain–Fritsch Convective Parameterization: An Update. *Journal of Applied Meteorology* **2004,** *43*, (1), 170-181.
16. Xiu, A.; Pleim, J. E., Development of a Land Surface Model. Part I: Application in a Mesoscale Meteorological Model. *Journal of Applied Meteorology* **2001,** *40*, (2), 192-209.
17. Pleim, J. E., A Combined Local and Nonlocal Closure Model for the Atmospheric Boundary Layer. Part II: Application and Evaluation in a Mesoscale Meteorological Model. *Journal of Applied Meteorology and Climatology* **2007,** *46*, (9), 1396-1409.
18. Iacono, M. J.; Delamere, J. S.; Mlawer, E. J.; Shephard, M. W.; Clough, S. A.; Collins, W. D., Radiative forcing by long-lived greenhouse gases: Calculations with the AER radiative transfer models. *Journal of Geophysical Research: Atmospheres* **2008,** *113*, (D13).
19. An, J.; Huang, Y.; Huang, C.; Wang, X.; Yan, R.; Wang, Q.; Wang, H.; Jing, S.; Zhang, Y.; Liu, Y.; Chen, Y.; Xu, C.; Qiao, L.; Zhou, M.; Zhu, S.; Hu, Q.; Lu, J.; Chen, C., Emission inventory of air pollutants and chemical speciation for specific anthropogenic sources based on local measurements in the Yangtze River Delta region, China. *Atmos. Chem. Phys.* **2021,** *21*, (3), 2003-2025.
20. Kurokawa, J.; Ohara, T.; Morikawa, T.; Hanayama, S.; Janssens-Maenhout, G.; Fukui, T.; Kawashima, K.; Akimoto, H., Emissions of air pollutants and greenhouse gases over Asian regions during 2000–2008: Regional Emission inventory in ASia (REAS) version 2. *Atmospheric Chemistry and Physics* **2013,** *13*, (21), 11019-11058.
21. Guenther, A.; Jiang, X.; Heald, C.; Sakulyanontvittaya, T.; Duhl, T.; Emmons, L.; Wang, X., The Model of Emissions of Gases and Aerosols from Nature Version 2.1 (MEGAN2.1): An extended and updated framework for modeling biogenic emissions. *Geoscientific Model Development* **2012,** *5*, 1471-1492.
22. Qiao, X.; Tang, Y.; Hu, J.; Zhang, S.; Li, J.; Kota, S. H.; Wu, L.; Gao, H.; Zhang, H.; Ying, Q., Modeling dry and wet deposition of sulfate, nitrate, and ammonium ions in Jiuzhaigou National Nature Reserve, China using a source-oriented CMAQ model: Part I. Base case model results. *The Science of the total environment* **2015,** *532*, 831-9.
23. Wiedinmyer, C.; Akagi, S. K.; Yokelson, R. J.; Emmons, L. K.; Al-Saadi, J. A.; Orlando, J. J.; Soja, A. J., The Fire INventory from NCAR (FINN): a high resolution global model to estimate the emissions from open burning. *Geoscientific Model Development* **2011,** *4*, (3), 625-641.
24. Shu, Z.; Liu, Y.; Zhao, T.; Xia, J.; Wang, C.; Cao, L.; Wang, H.; Zhang, L.; Zheng, Y.; Shen, L.; Luo, L.; Li, Y., Elevated 3D structures of PM_{2.5} and impact of complex terrain-forcing circulations on heavy haze pollution over

Sichuan Basin, China. *Atmospheric Chemistry and Physics* **2021,** *21*, (11), 9253-9268.
25. Emery, C.; Tai, E. In *Enhanced Meteorological Modeling and Performance Evaluation for Two Texas Ozone Episodes*, 2001; 2001.
26. Emery, C.; Liu, Z.; Russell, A.; Odman, M.; Yarwood, G.; Kumar, N., Recommendations on Statistics and Benchmarks to Assess Photochemical Model Performance. *Journal of the Air & Waste Management Association (1995)* **2016,** *67*.
27. Yin, Z.; Wan, Y.; Zhang, Y.; Wang, H., Why super sandstorm 2021 in North China. *National science review* **2021**.
28. Fan, K.; Xie, Z.; Wang, H.; Xu, Z.; Liu, J., Frequency of spring dust weather in North China linked to sea ice variability in the Barents Sea. *Climate Dynamics* **2017,** *51*, (11-12), 4439-4450.
29. Wang, Z.; Huang, X.; Wang, N.; Xu, J.; Ding, A., Aerosol-Radiation Interactions of Dust Storm Deteriorate Particle and Ozone Pollution in East China. *Journal of Geophysical Research: Atmospheres* **2020,** *125*, (24).
30. Hu, J.; Li, Y.; Zhao, T.; Liu, J.; Hu, X.-M.; Liu, D.; Jiang, Y.; Xu, J.; Chang, L., An important mechanism of regional O₃ transport for summer smog over the Yangtze River Delta in eastern China. *Atmospheric Chemistry and Physics* **2018,** *18*, (22), 16239-16251.
31. Gao, J.; Zhu, B.; Xiao, H.; Kang, H.; Hou, X.; Shao, P., A case study of surface ozone source apportionment during a high concentration episode, under frequent shifting wind conditions over the Yangtze River Delta, China. *Science of The Total Environment* **2016,** *544*, 853-863.
32. Wang, D.; Zhou, B.; Fu, Q.; Zhao, Q.; Zhang, Q.; Chen, J.; Yang, X.; Duan, Y.; Li, J., Intense secondary aerosol formation due to strong atmospheric photochemical reactions in summer: observations at a rural site in eastern Yangtze River Delta of China. *Science of The Total Environment* **2016,** *571*, 1454-1466.
33. Zhao, D.; Liu, G.; Xin, J.; Quan, J.; Wang, Y.; Wang, X.; Dai, L.; Gao, W.; Tang, G.; Hu, B.; Ma, Y.; Wu, X.; Wang, L.; Liu, Z.; Wu, F., Haze pollution under a high atmospheric oxidization capacity in summer in Beijing: insights into formation mechanism of atmospheric physicochemical processes. *Atmospheric Chemistry and Physics* **2020,** *20*, (8), 4575-4592.
34. Ma, Y.; Ye, J.; Xin, J.; Zhang, W.; Vilà-Guerau de Arellano, J.; Wang, S.; Zhao, D.; Dai, L.; Ma, Y.; Wu, X.; Xia, X.; Tang, G.; Wang, Y.; Shen, P.; Lei, Y.; Martin, S. T., The Stove, Dome, and Umbrella Effects of Atmospheric Aerosol on the Development of the Planetary Boundary Layer in Hazy Regions. *Geophysical Research Letters* **2020,** *47*, (13).
35. Shen, L.; Zhao, C., Dominance of Shortwave Radiative Heating in the Sea-Land Breeze Amplitude and its Impacts on Atmospheric Visibility in Tokyo, Japan. *Journal of Geophysical Research: Atmospheres* **2020,** *125*, (8).
36. Xing, J.; Wang, J.; Mathur, R.; Pleim, J.; Wang, S.; Hogrefe, C.; Gan, C. M.; Wong, D. C.; Hao, J., Unexpected Benefits of Reducing Aerosol Cooling Effects. *Environmental science & technology* **2016,** *50*, (14), 7527-34.
37. Ding, A. J.; Huang, X.; Nie, W.; Sun, J. N.; Kerminen, V. M.; Petäjä, T.; Su, H.; Cheng, Y. F.; Yang, X. Q.; Wang, M. H.; Chi, X. G.; Wang, J. P.; Virkkula, A.; Guo, W. D.; Yuan, J.; Wang, S. Y.; Zhang, R. J.; Wu, Y. F.; Song, Y.; Zhu, T.; Zilitinkevich, S.; Kulmala, M.; Fu, C. B., Enhanced haze pollution by black carbon in megacities in China. *Geophysical Research Letters* **2016,** *43*, (6), 2873-2879.
38. Jung, J.; Souri, A. H.; Wong, D. C.; Lee, S.; Jeon, W.; Kim, J.; Choi, Y., The Impact of the Direct Effect of Aerosols on Meteorology and Air Quality Using Aerosol Optical Depth Assimilation During the KORUS-AQ Campaign. *Journal of Geophysical Research: Atmospheres* **2019,** *124*, (14), 8303-8319.
39. Wang, J.; Wang, S.; Jiang, J.; Ding, A.; Zheng, M.; Zhao, B.; Wong, D. C.; Zhou, W.; Zheng, G.; Wang, L.; Pleim, J. E.; Hao, J., Impact of aerosol–meteorology interactions on fine particle pollution during China's severe haze episode in January 2013. *Environmental Research Letters* **2014,** *9*, (9), 094002.
40. Gao, Y.; Zhang, M.; Liu, Z.; Wang, L.; Wang, P.; Xia, X.; Tao, M.; Zhu, L., Modeling the feedback between aerosol and meteorological variables in the atmospheric boundary layer during a severe fog–haze event over the North China Plain. *Atmos. Chem. Phys.* **2015,** *15*, (8), 4279-4295.
41. Wang, H.; Shi, G. Y.; Zhang, X. Y.; Gong, S. L.; Tan, S. C.; Chen, B.; Che, H. Z.; Li, T., Mesoscale modelling study of the interactions between aerosols and PBL meteorology during a haze episode in China Jing–Jin–Ji and its near surrounding region – Part 2: Aerosols' radiative feedback effects. *Atmos. Chem. Phys.* **2015,** *15*, (6), 3277-3287.
42. Gao, M.; Carmichael, G. R.; Wang, Y.; Saide, P. E.; Yu, M.; Xin, J.; Liu, Z.; Wang, Z., Modeling study of the 2010 regional haze event in the North China Plain. *Atmos. Chem. Phys.* **2016,** *16*, (3), 1673-1691.
43. Liu, Q.; Jia, X.; Quan, J.; Li, J.; Li, X.; Wu, Y.; Chen, D.; Wang, Z.; Liu, Y., New positive feedback mechanism between boundary layer meteorology and secondary aerosol formation during severe haze events. *Scientific reports* **2018,** *8*, (1), 6095.

44. Zhang, X.; Zhang, Q.; Hong, C.; Zheng, Y.; Geng, G.; Tong, D.; Zhang, Y.; Zhang, X., Enhancement of PM2.5 Concentrations by Aerosol-Meteorology Interactions Over China. *Journal of Geophysical Research: Atmospheres* **2018,** *123*, (2), 1179-1194.
45. Wu, J.; Bei, N.; Hu, B.; Liu, S.; Zhou, M.; Wang, Q.; Li, X.; Liu, L.; Feng, T.; Liu, Z.; Wang, Y.; Cao, J.; Tie, X.; Wang, J.; Molina, L. T.; Li, G., Aerosol–radiation feedback deteriorates the wintertime haze in the North China Plain. *Atmospheric Chemistry and Physics* **2019,** *19*, (13), 8703-8719.

Table and Figures

Table S1 Statistics metrics of comparison between observed (Obs) and simulated (Sim) for meteorological conditions (temperature at 2 m (T2), wind speed at 10 m (WS10), wind direction at 10 m (WD10), and relative humidity (RH)) with the correlation coefficient (R), mean bias (MB), mean error (ME), and root mean squared error (RMSE) from 31 March to 10 April 2019.

	Obs	**Sim**	**MB**	**ME**	**RMSE**	**Benchmark**
T2 (°C)	15.69	14.62	-1.07	1.93	2.43	MB≤±0.5;ME≤2.0
RH (%)	65.59	64.62	-0.97	7.43	8.82	
WD (degree)	169.68	168.74	-0.94	26.75	35.10	MB≤±10;ME≤30.0
WS (m/s)	2.74	3.01	0.26	0.56	0.67	MB≤±0.5;ME≤2.0; RMSE ≤2.0

Table S2 Statistics metrics of comparison between observed and simulated surface $PM_{2.5}$ and O_3 concentrations with normalized mean bias (NMB), normalized mean error (NME), correlation coefficient (R), and an index of agreement (IOA) during 31 March-10 April 2019.

	Obs	Sim	R	IOA	NMB	NME	Bechmark
$PM_{2.5}$ (μg/m^3)	45.17	49.4	0.87	0.91	0.09	0.21	NMB≤±0.3;NME≤0.5
O_3 (ppb)	39.6	41.97	0.91	0.94	0.06	0.19	NMB≤±0.15;NME≤0.3

Table S3. Effects of ADRE (YFb-NoFb) on the daily average of $PM_{2.5}$ and O_3 in the eight cities (urban area) on DHP days.

	MDA8 O_3 (μg/m^3)			Avg O_3 (μg/m^3)			Avg $PM_{2.5}$ (μg/m^3)		
	YFb	NoFb	ADRE	YFb	NoFb	ADRE	YFb	NoFb	ADRE
Yancheng	168.2	170.9	-4.8	90.4	95.0	-5.8	101.4	98.2	3.2
Shanghai	171.5	171.5	0	105.3	105.6	-0.3	85.2	81.2	4.0
Suzhou	213.3	193.8	10.2	94.4	93.1	1.3	89.3	86.8	2.5
Changzhou	197.6	180.5	13.0	117.0	114.9	2.1	84.6	78.8	5.8
Nanjing	212. 1	208.0	4.1	139.6	140.6	-1.0	100.9	92.5	8.4
Chuzhou	218.0	196.9	21.1	135.8	129.4	6.4	96.7	85.8	10.9
Hangzhou	173.3	169.6	3.7	105.6	110.0	-4.4	63.9	66.6	-2.7
Shaoxing	187.9	179.8	8.1	120.9	116.7	4.2	49.9	47.3	2.6

Table S4. Effects of aerosol radiative feedback on near-surface $PM_{2.5}$ in China

Reference	Time	Location	Impact on $PM_{2.5}$
In this study	5-8 April 2019	The 8 cities with DHP in the YRD rgion	+4.3 μg/m^3 (+5.4%)
Wang, et al. [39]	January 2013	North China Plain	+22.7 μg/m^3
Gao, et al. [40]	10-15 January 2013	Beijing、Tianjin and south Hebei	+10-50 μg/m^3
Wang, et al. [41]	7-11 July 2008	North China Plain	+14 %
Ding et al.	December 2013	Eastern China and the Sichuan Basin	hourly maximum +100 μg/m^3
Gao, et al. [42]	January 2010	Shijiazhuang	More than +20 μg/m^3
Liu, et al. [43]	15-16 December 2016	North China Plain	+56 μg/m^3
Zhang, et al. [44]	2014	China	Over +16 % for the daily maximum $PM_{2.5}$
Wu, et al. [45]	5 December 2015-4 January 2016	North China Plain	+10.2 μg/m^3 (+7.8%)

Table S5. Effects of ADRE (YFb-NoFb) on the source and sink of O_3 physical and chemical processes in the boundary layer of the eight cities (the administrative region) on DHP days

	ΔCHEM (μg/m^3)		ΔDDEP (μg/m^3)		ΔHTRA (μg/m^3)		ΔVMIX (μg/m^3)	
	Source	Sink	Source	Sink	Source	Sink	Source	Sink
Yancheng	18.3	-1.4	0	1.3	9.3	6.2	15.6	0
Shanghai	13.3	-6.3	0	7.4	-2.5	0.1	19.6	0
Suzhou	9.9	3.2	0	15.8	-3.9	-8.7	17.1	0
Changzhou	9.5	-4.2	0	9	-0.7	4.7	31.7	0
Nanjing	28	3.8	0	22	4.5	2	20.6	0
Chuzhou	19.2	1.8	0	32	-15.3	18.3	20.9	0
Hangzhou	5.9	-2.7	0	13.7	2.5	1	15.1	-0.5
Shaoxing	8.1	2	0	43.1	-2.1	1.9	46.2	-0.6

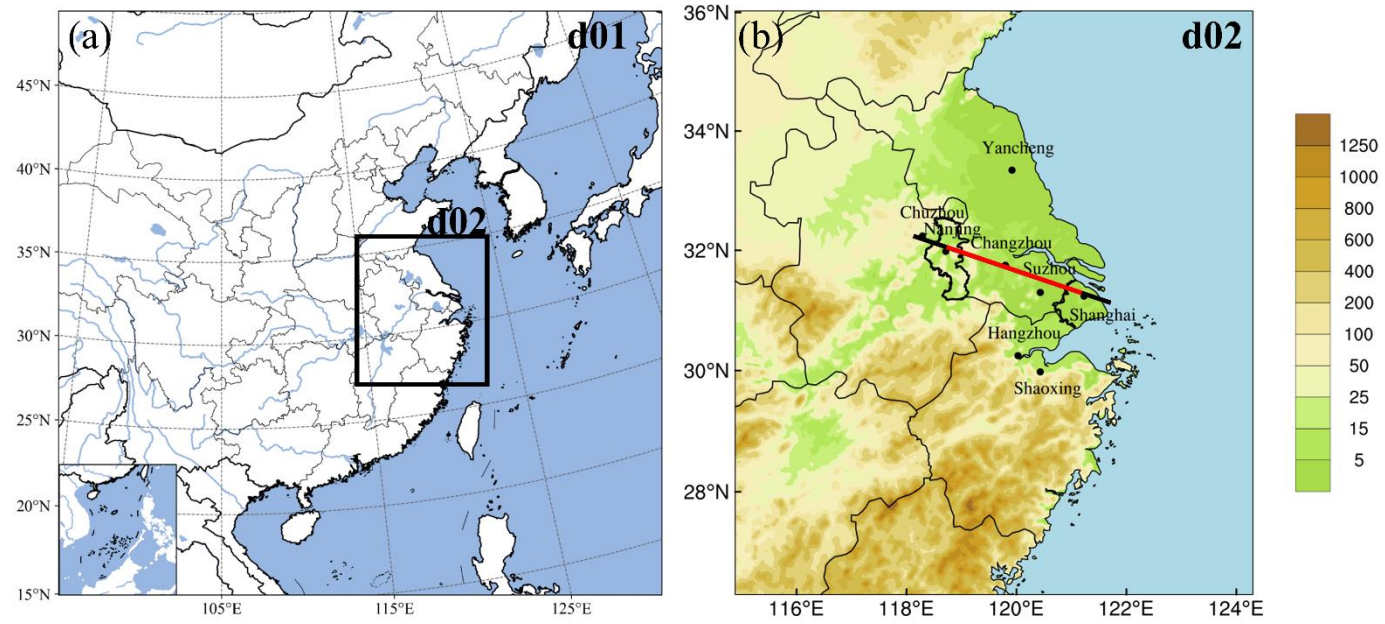


Figure S1. (a) The two nesting domains for the CMAQ simulation. (b) The topography with respect to altitude (m) and the locations of the eight cities with DHP over the YRD in the innermost domain, d02. The black line in Figure 1b is the regional transmission path, and the red line in Figure 1b is the Shanghai-Nanjing transmission pathway.

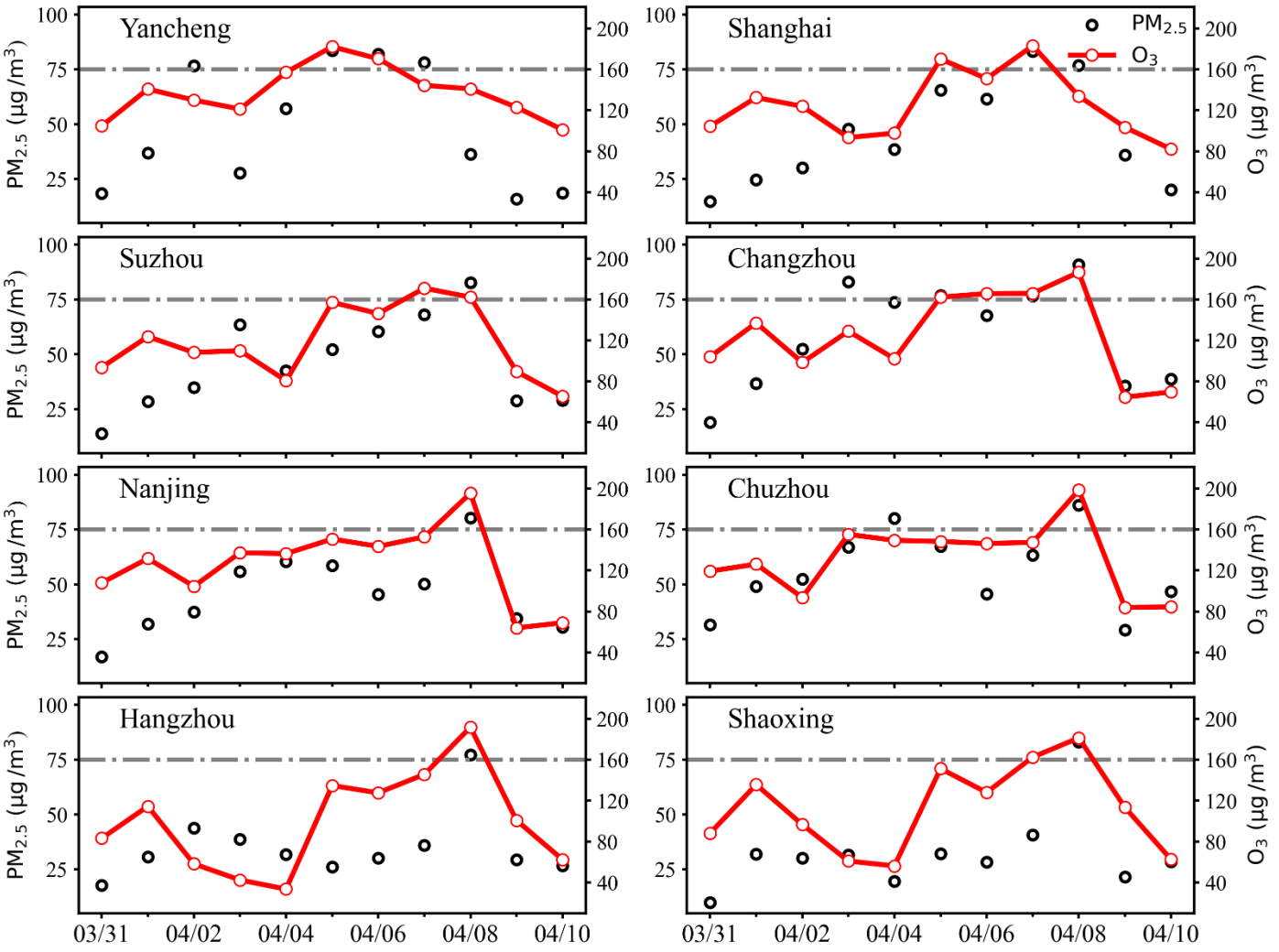


Figure S2. Time series of $PM_{2.5}$ daily average and MDA8 O_3 in the eight cities with DHP in the YRD from 31 March to 10 April, 2019

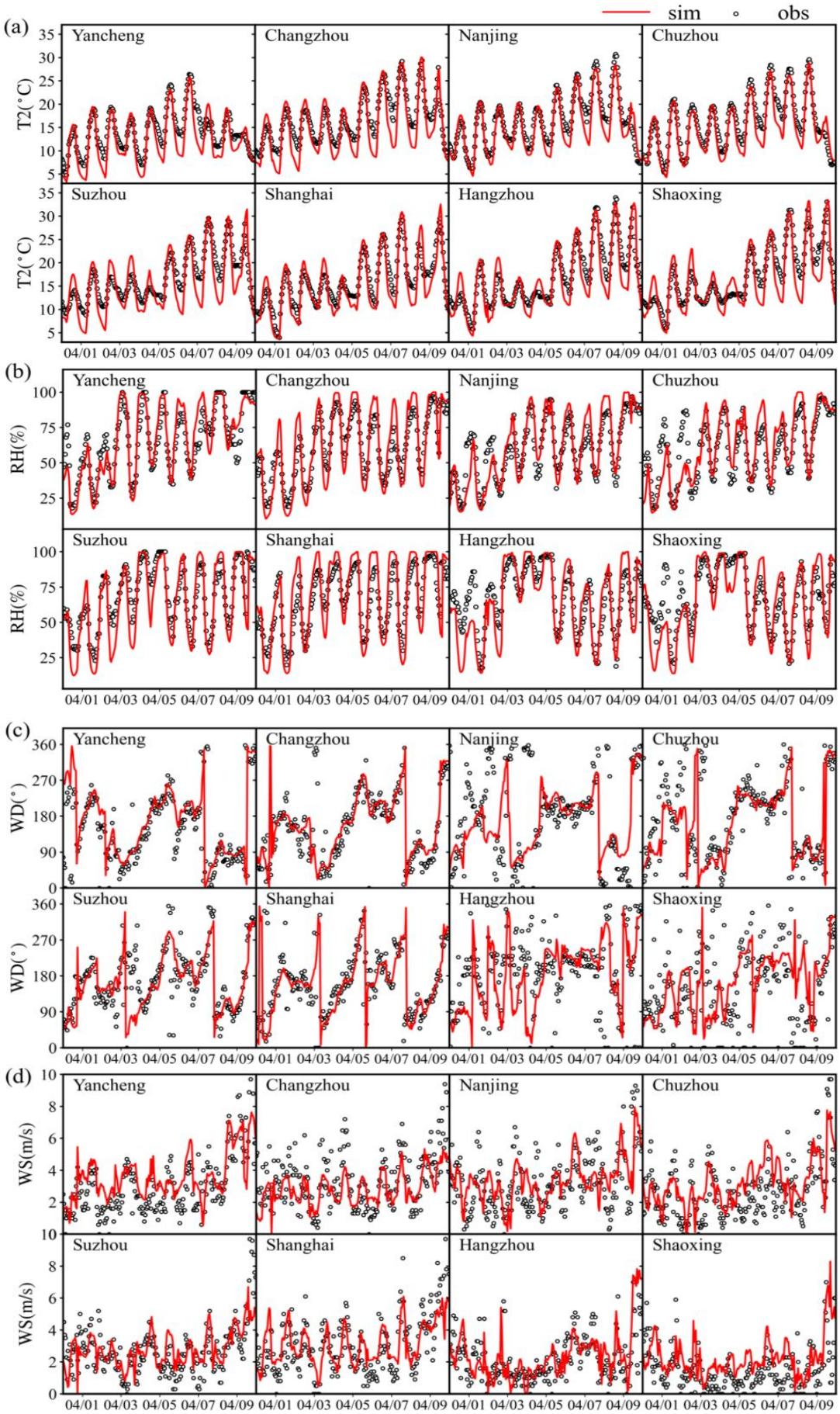


Figure S3. Hourly variations of observed (black dots) and simulated (red curves) of (a) 2m air temperature (T2), (b) relative humidity (RH), (c) 10 wind direction (WD) and (d) wind speed (WS) in the eight DHP cities during the study period.

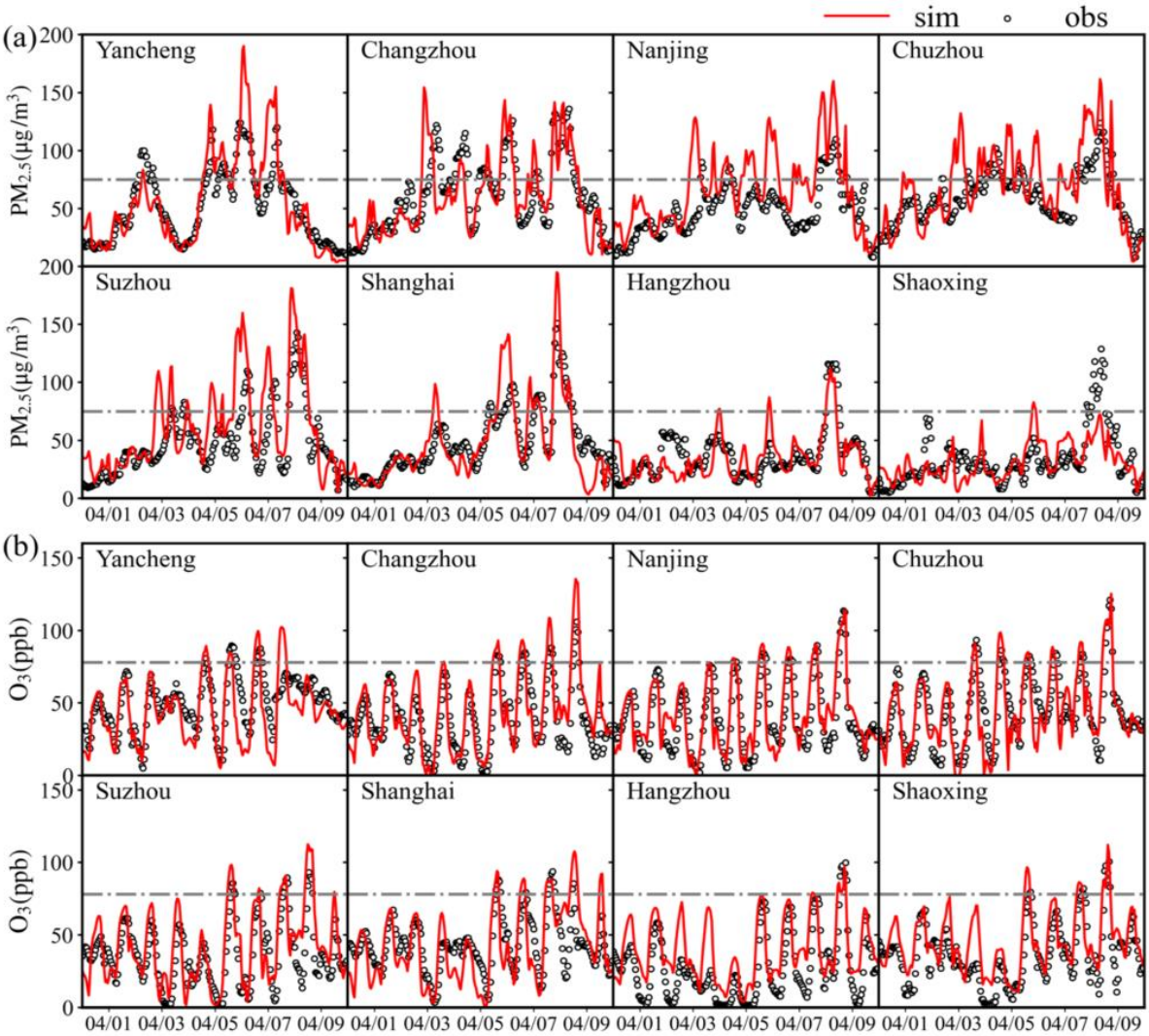


Figure S4. Hourly variation of observed (black dots) and simulated (red curves) of $PM_{2.5}$ and O_3 in the eight DHP cities during the study period.

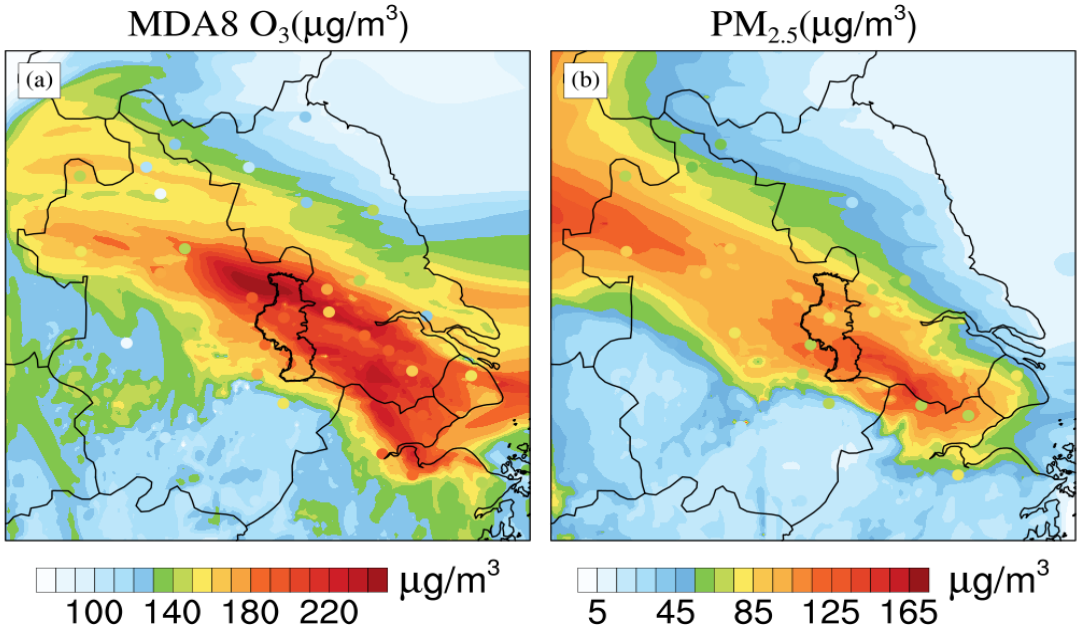


Figure S5. Spatial distribution of daily average $PM_{2.5}$ and MDA8 O_3 on 8 April (the regional DHP day). The scatter plot contained the observed values of the daily average of $PM_{2.5}$ and MDA8 O_3 for 34 cities in the YRD region on 8 April.

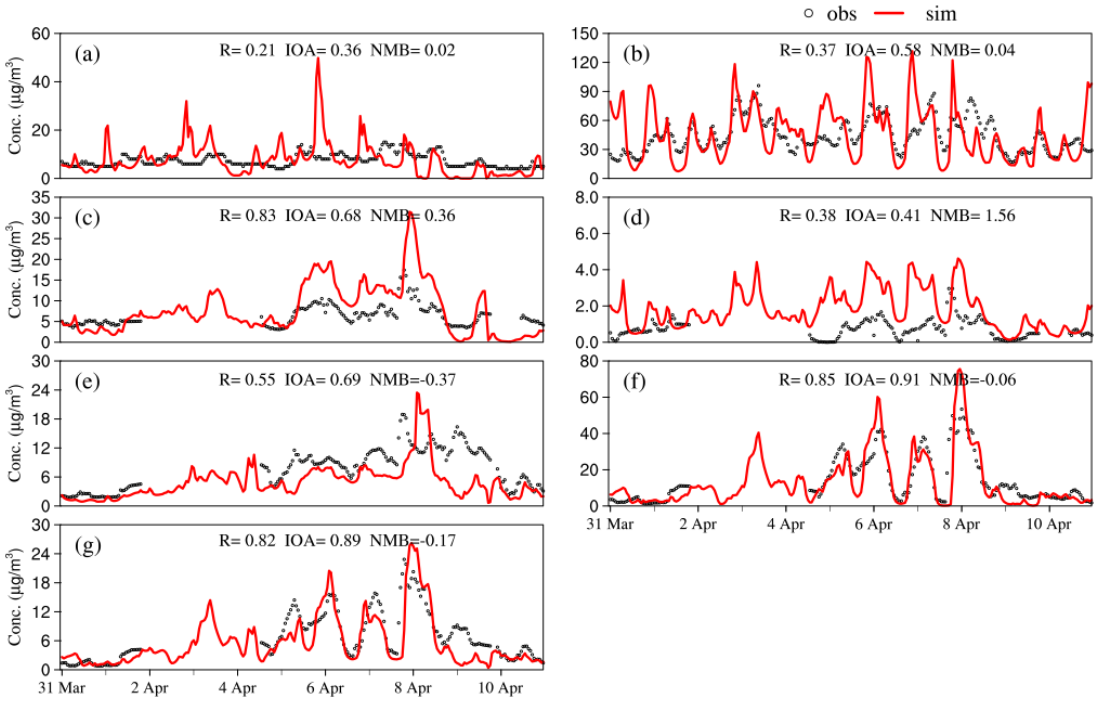


Figure S6. Hourly variations of observed (black dots) and simulated (red curves) (a) SO_2, (b) NO_2, (c) OC, (d) EC, (e) SO_4^{2-}, (f) NO_3^-, and (g) NH_4^+ respectively in Shanghai during the study period.

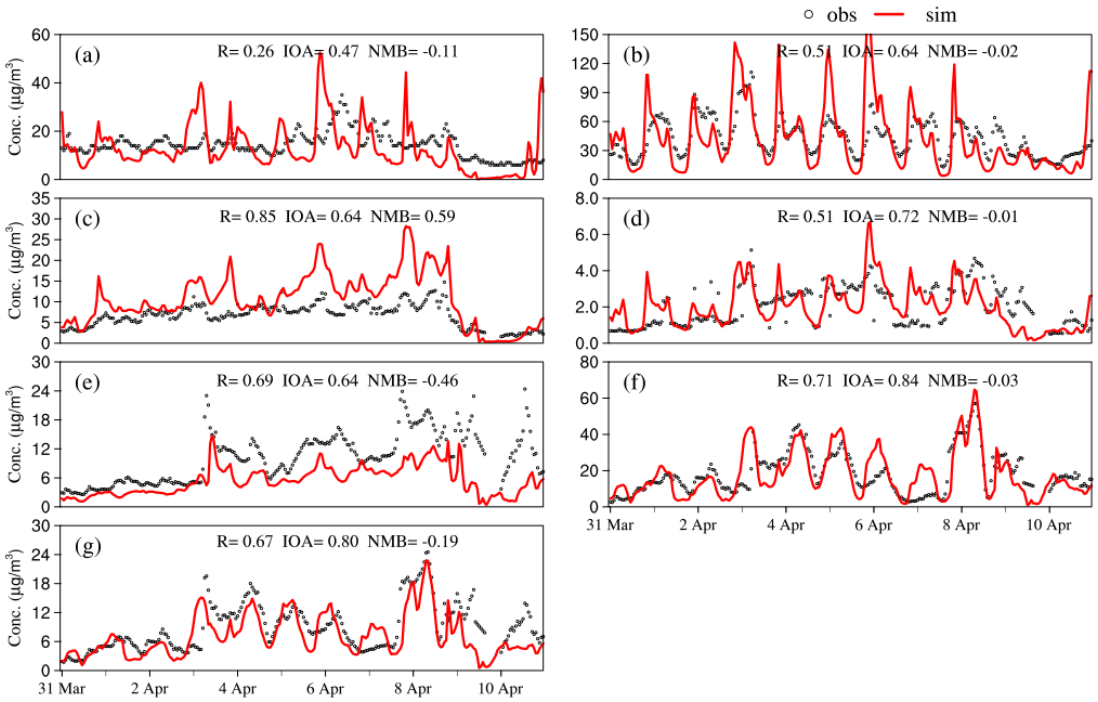


Figure S7. Same as Figure S6, but for Nanjing.

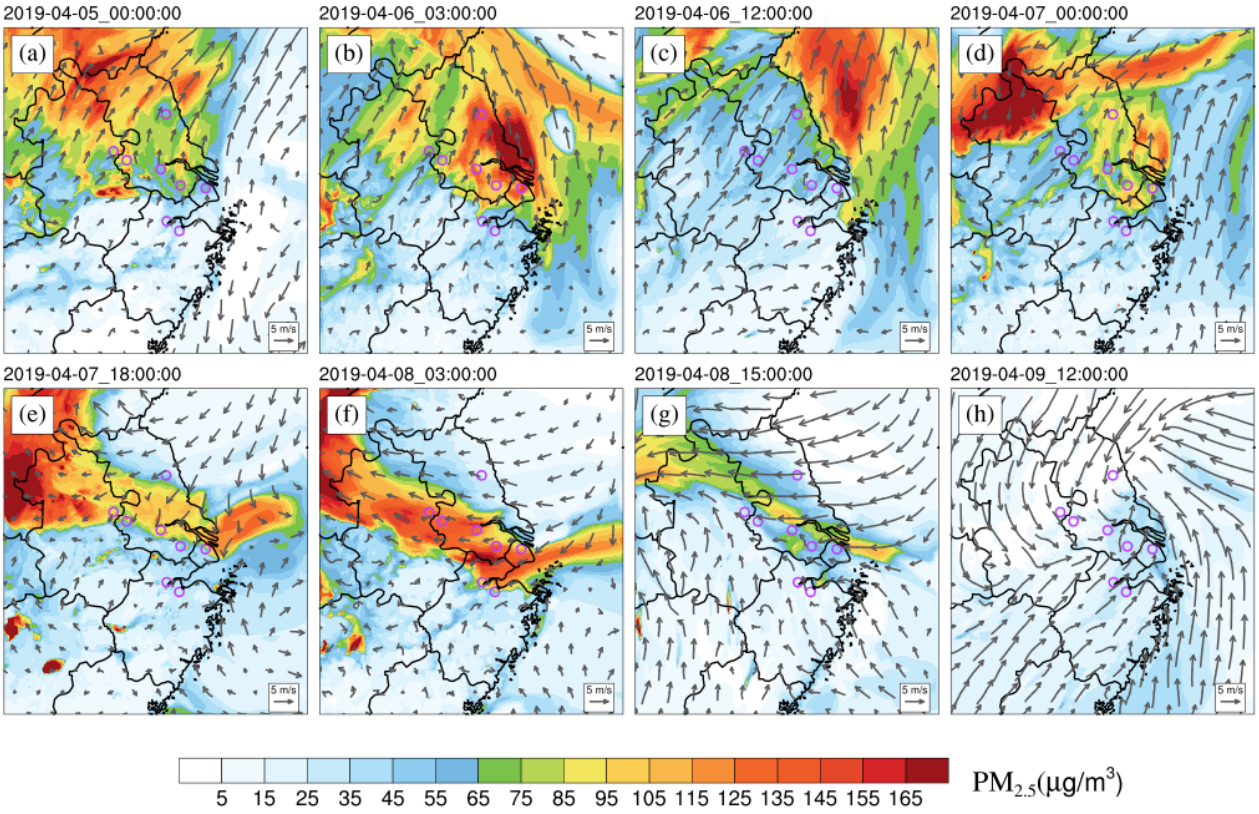


Figure S8. Spatial distribution of $PM_{2.5}$ concentrations (color-filled contours) and wind vectors (arrows) at (a) 00:00 LT on 5 April, (b) 03:00 LT on 6 April, (c) 12:00 LT on 6 April, (d) 00:00 LT on 7 April, (e) 18:00 LT on 7 April, (f) 03:00 LT on 8 April, (g) 15:00 LT on 8 April, (h) 12:00 LT on 9 April.

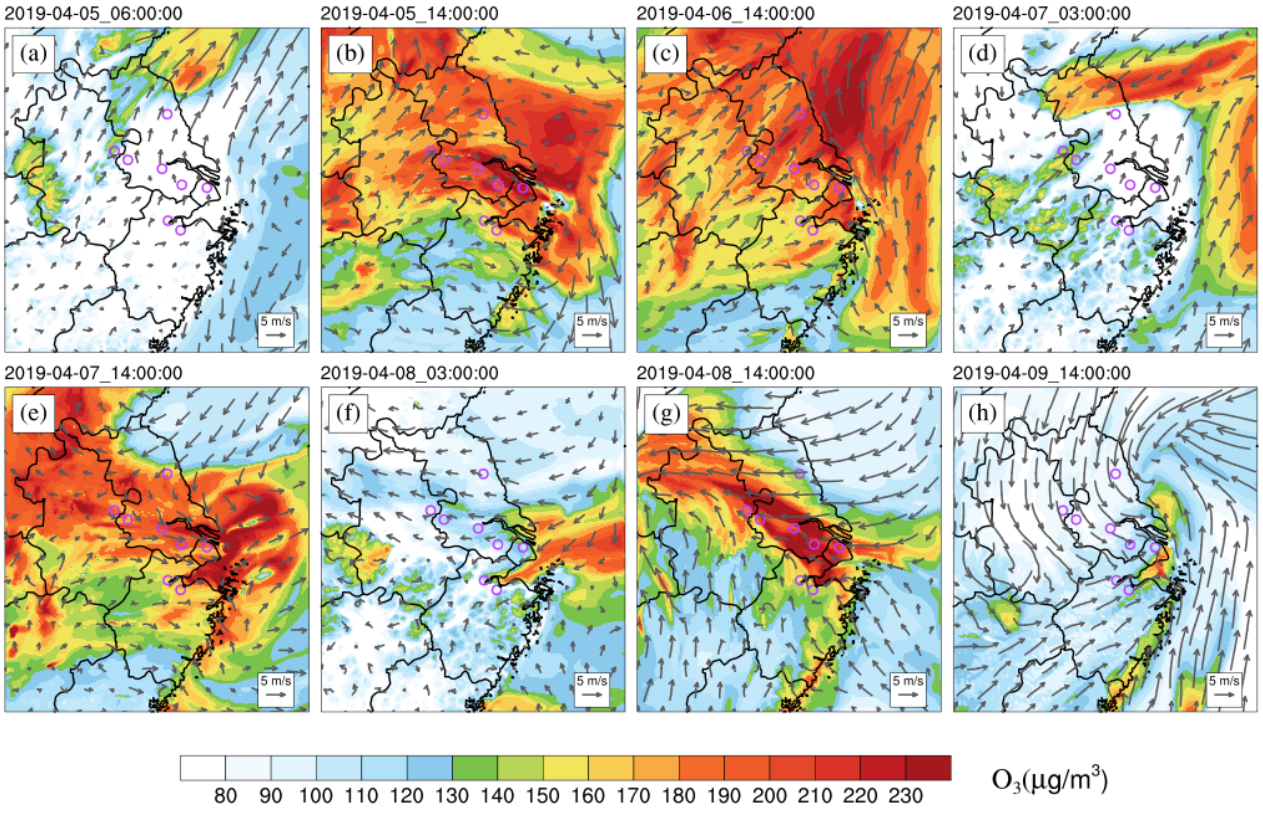


Figure S9. Spatial distribution of O_3 concentrations (color-filled contours) and wind vectors (arrows) at (a) 06:00 LT on 5 April, (b) 14:00 LT on 6 April, (c) 14:00 LT on 6 April, (d) 03:00 LT on 7 April, (e) 14:00 LT on 7 April, (f) 03:00 LT on 8 April, (g) 14:00 LT on 8 April, (h) 14:00 LT on 9 April.

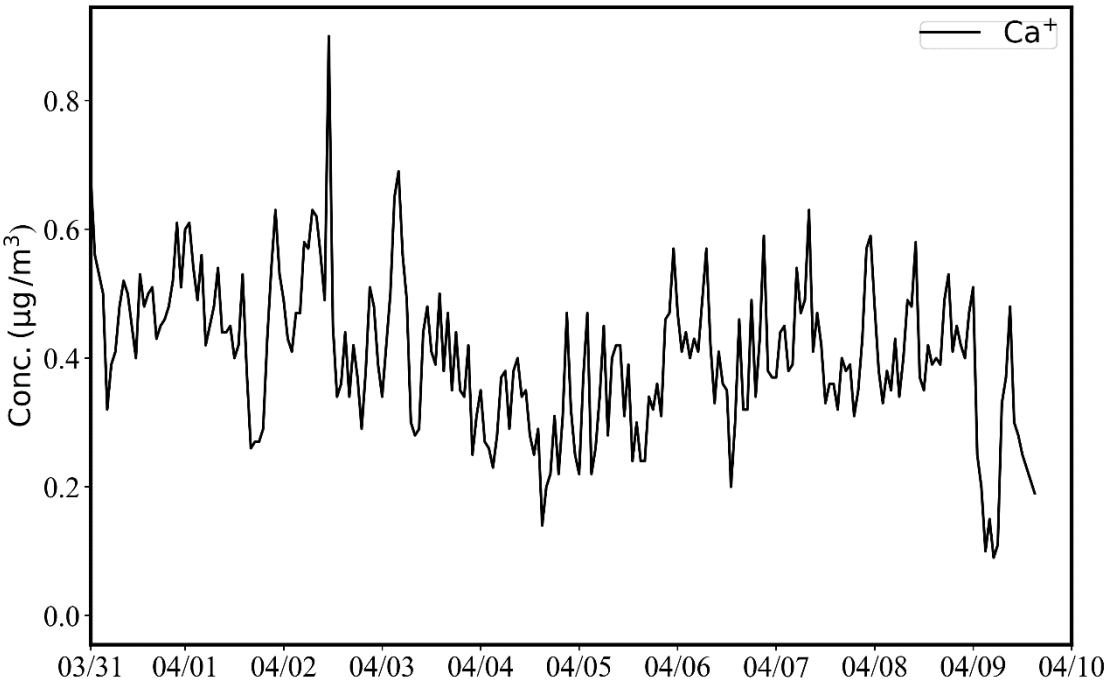


Figure S10. Hourly observations of Ca^{+} in Nanjing during the study period.

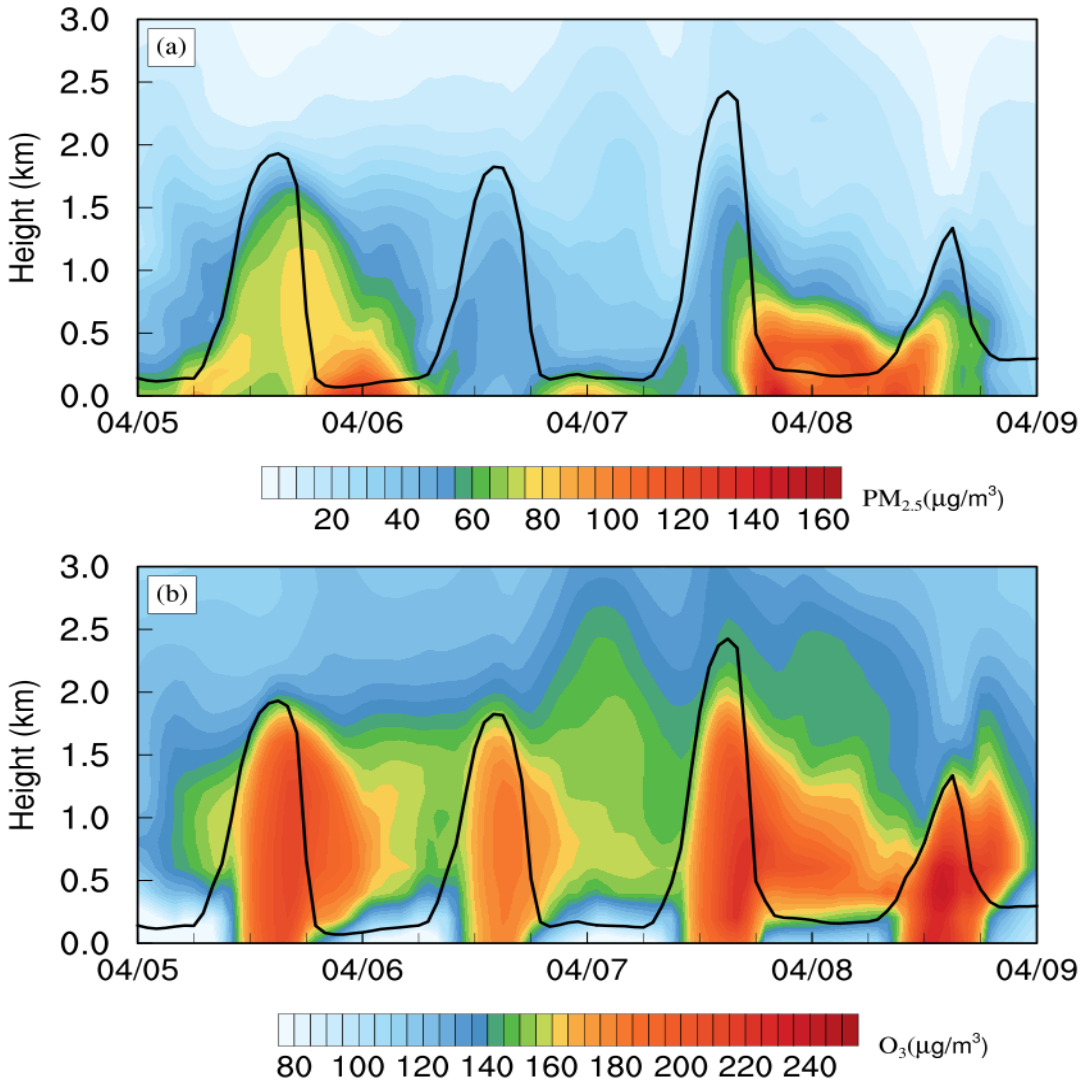


Figure S11. Time-altitude cross sections of $PM_{2.5}$ (a) and O_3 (b) concentrations along the Shanghai-Nanjing transport path (black solid line in Figure S1b) on 5-9 April, with the black line indicating the time series of PBL height.

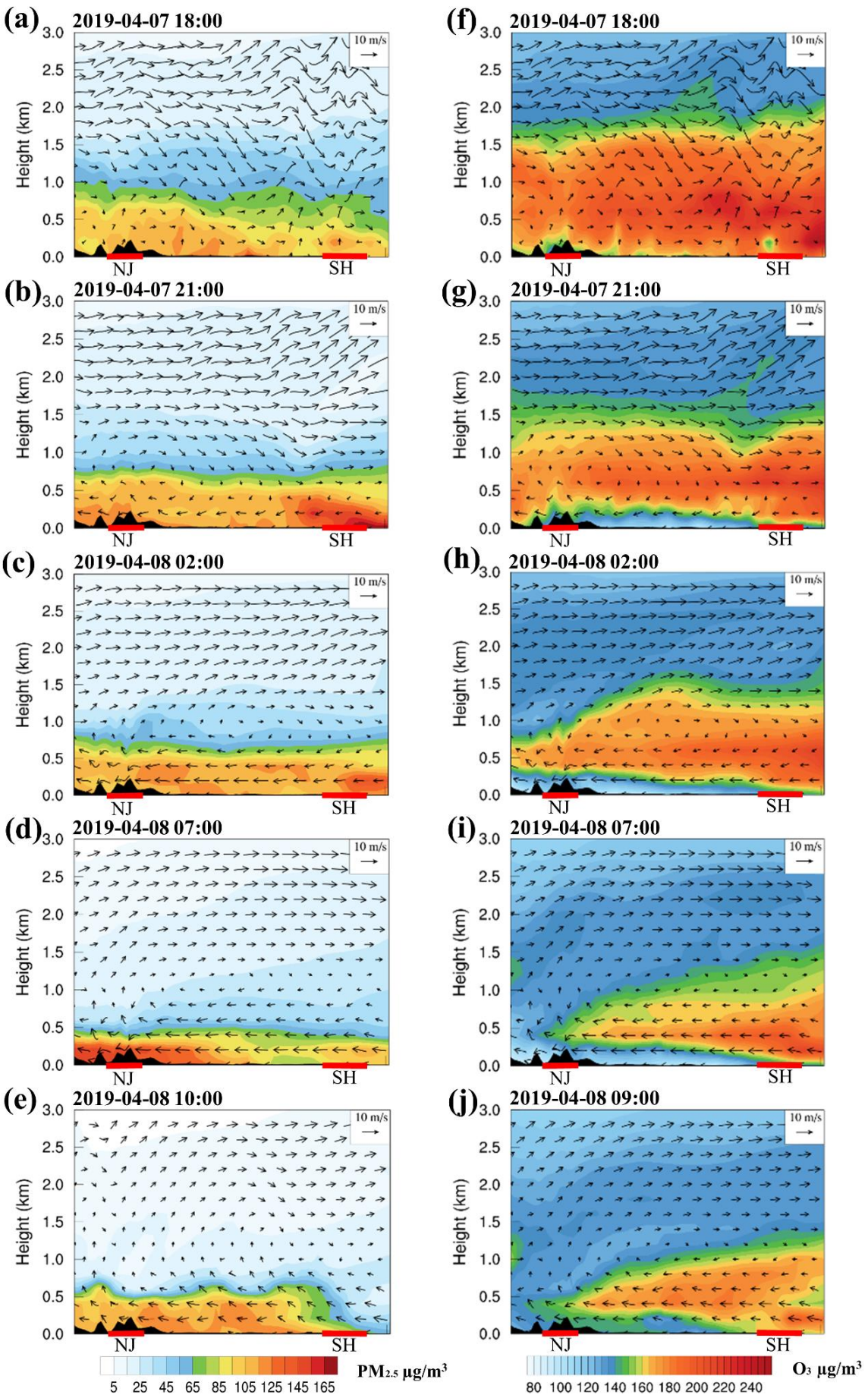


Figure S12. Vertical sections of $PM_{2.5}$ (a-e) and O_3 (f-j) concentration (contours) and atmospheric circulation (wind vector) at different times along the regional transport path. The vertical wind velocities are multiplied by 20 for the illustration of vertical circulations.

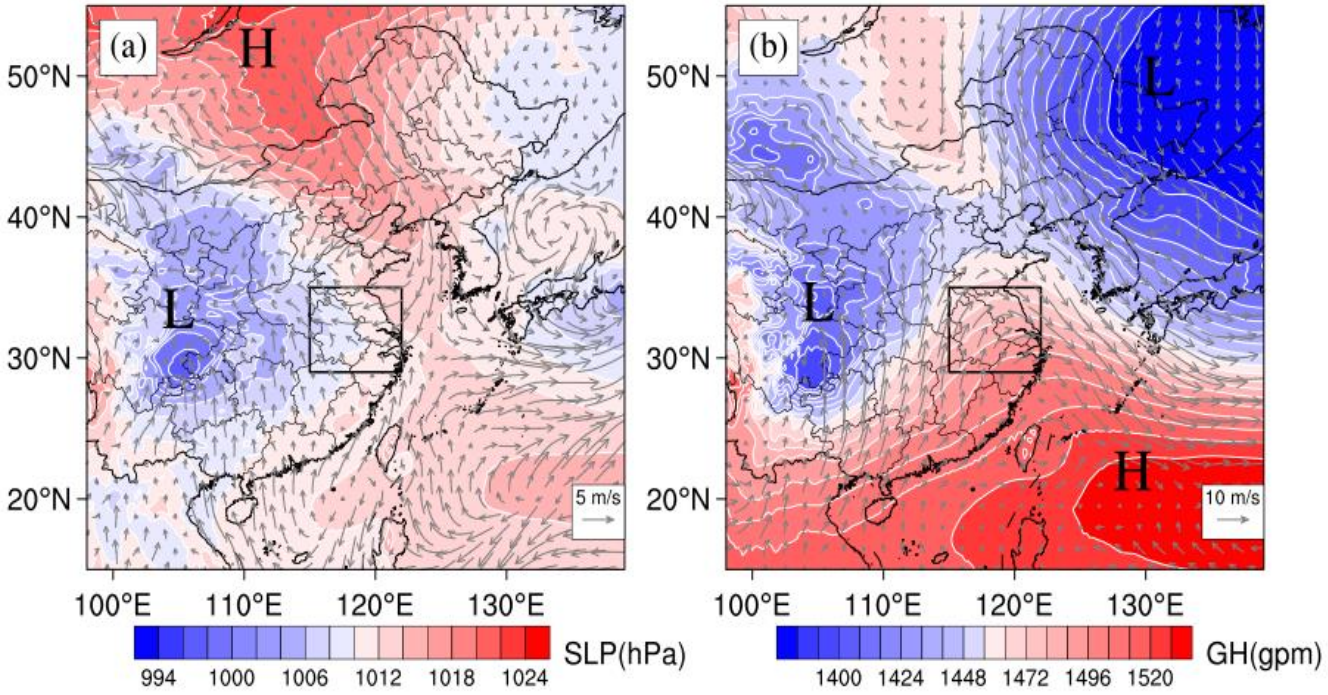


Figure S13. The synoptic situation of the sea level pressure (SLP) and the geopotential height of 850hPa from 18:00 on 7 April to 08:00 on 8 April.(The data was obtained from ECMWF)

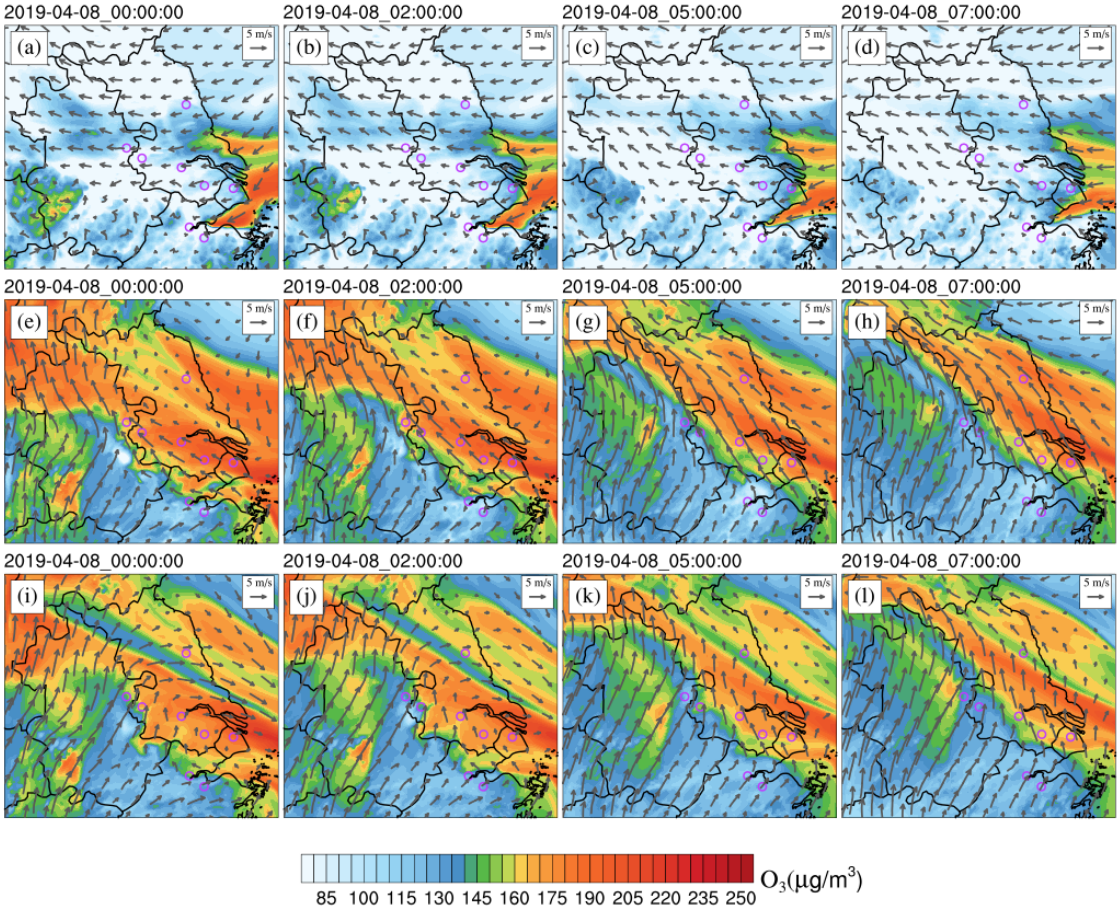


Figure S14. The spatial distribution of O_3 concentrations and wind vectors at a height surface at (a) 00:00, (b) 02:00, (c) 05:00, (d) 07:00, about 500m at (e) 00:00, (f) 02:00, (g) 05:00, (h) 07:00 and about 900m at (i) 00:00, (j) 02:00, (k) 05:00, (l) 07:00 on 8 April 2019.

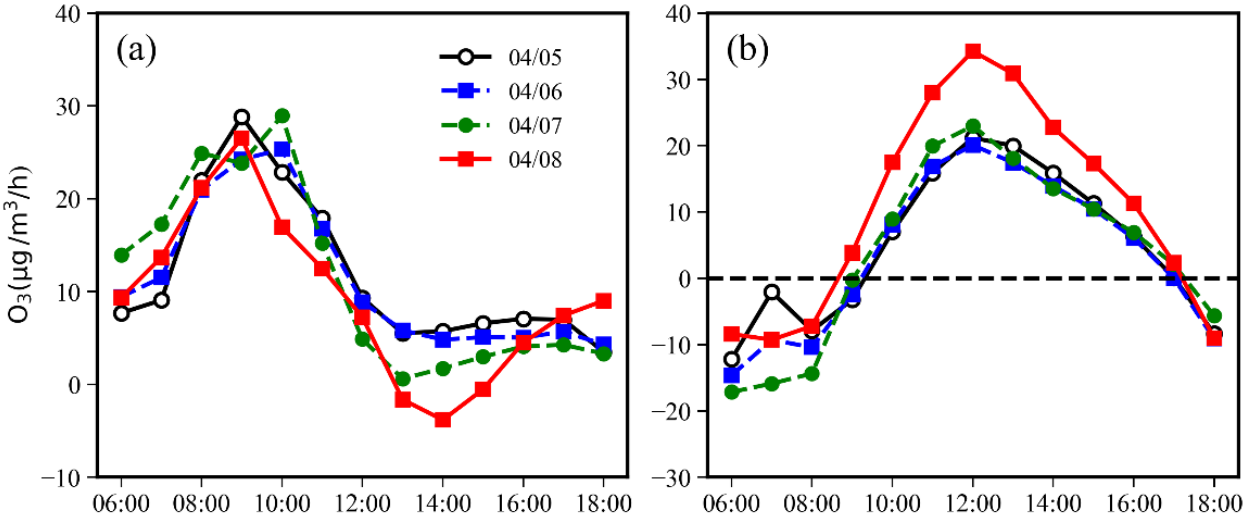


Figure S15. The time series of vertical mixing (a) and photochemical process (b) in the PBL along the Shanghai-Nanjing transport path during the daytime on 5-8 April.

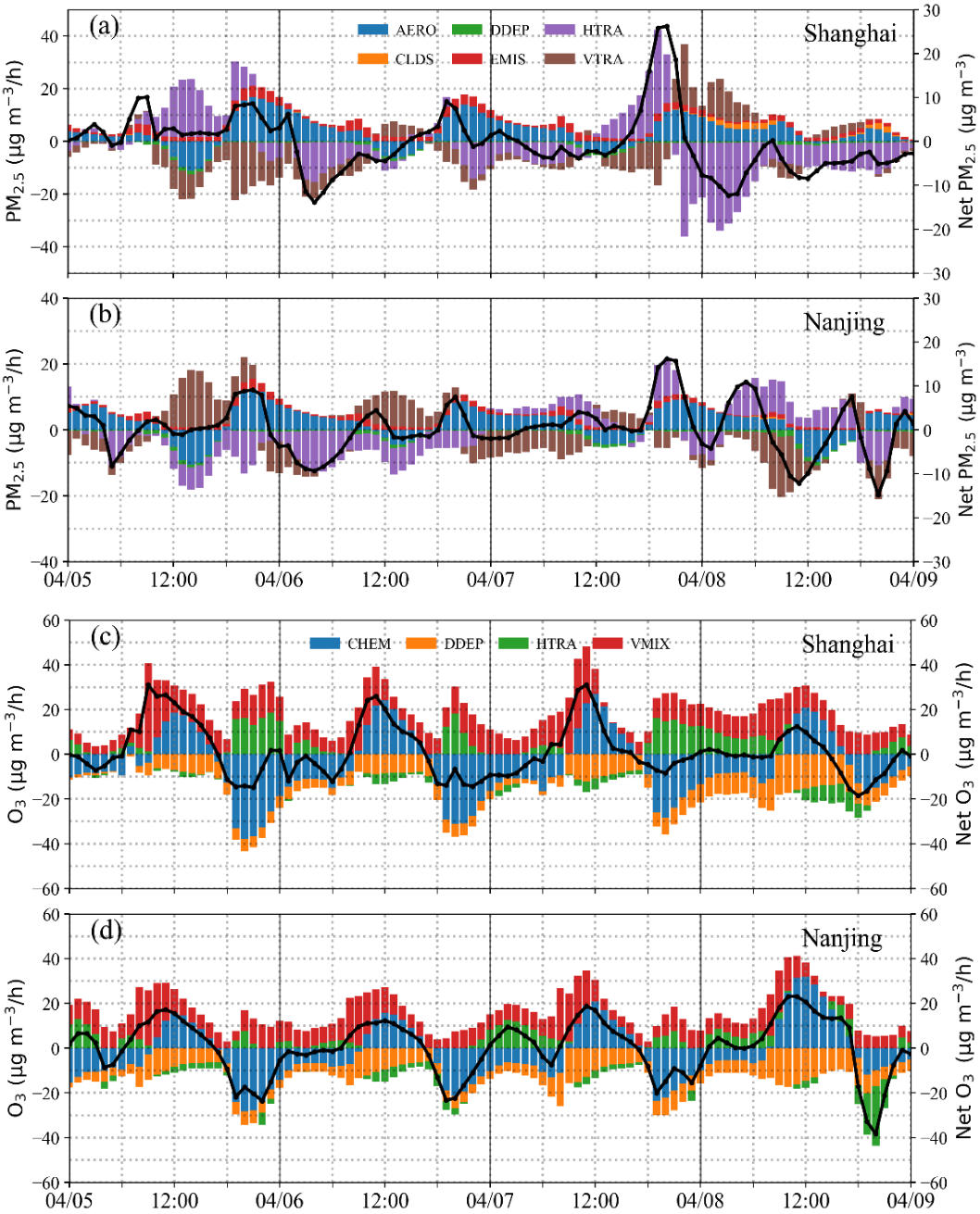


Figure S16 Hourly mean contributions of $PM_{2.5}$ in the PBL over (a) Shanghai (administrative region) and (b) Nanjing (administrative region) by using the IPR analysis method on 5-9 April, with the black line indicating the hourly net $PM_{2.5}$ change in the PBL. AERO, DDEP, HTRA, CLDS, EMIS, and VTRA mean aerosol process, dry deposition, horizontal transport, cloud process, emission process, and vertical transport process in $PM_{2.5}$, respectively. Hourly mean contributions of O_3 in the PBL over (c) Shanghai (administrative region) and (d) Nanjing (administrative region) by using the IPR analysis method on 5-9 April, with the black line indicating the hourly net O_3 change in the PBL. CHEM, DDEP, HTRA and VMIX mean photochemical process, dry deposition, horizontal transport, and vertical mixing.

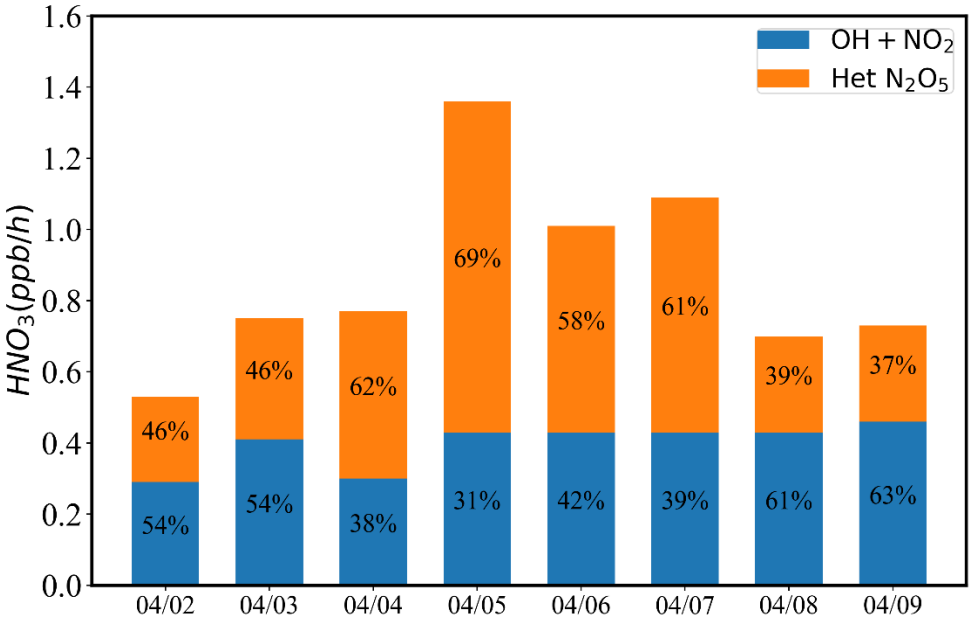


Figure S17. The histogram of the average daily values of the homogenous reaction ($OH+NO_2$) and heterogeneous reaction (Het N_2O_5) on 2-9 April in Shanghai area.

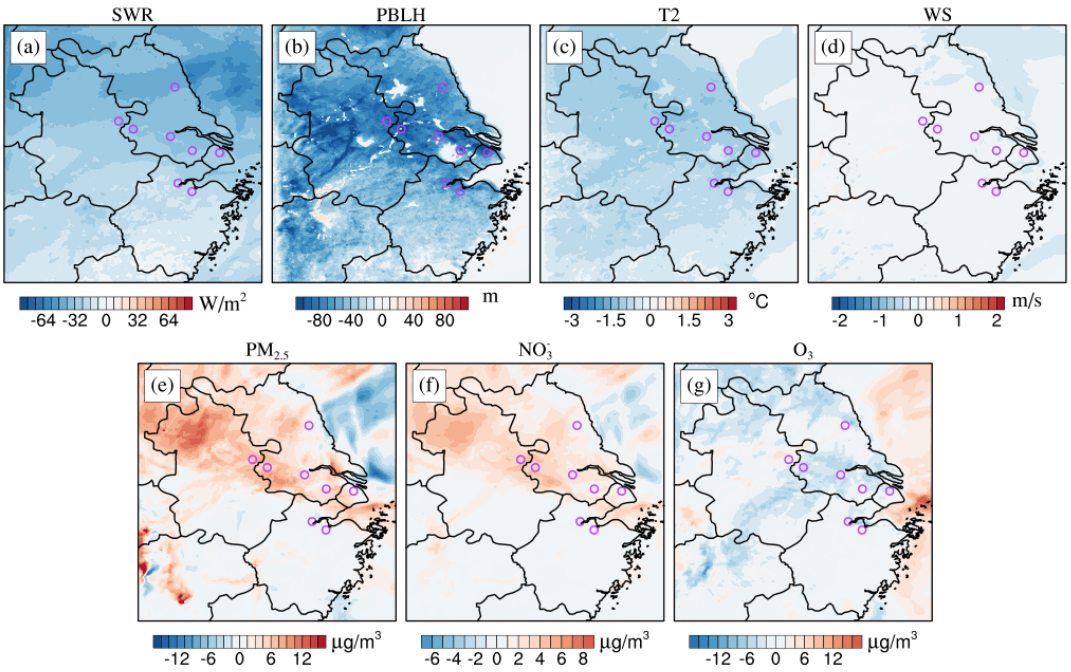
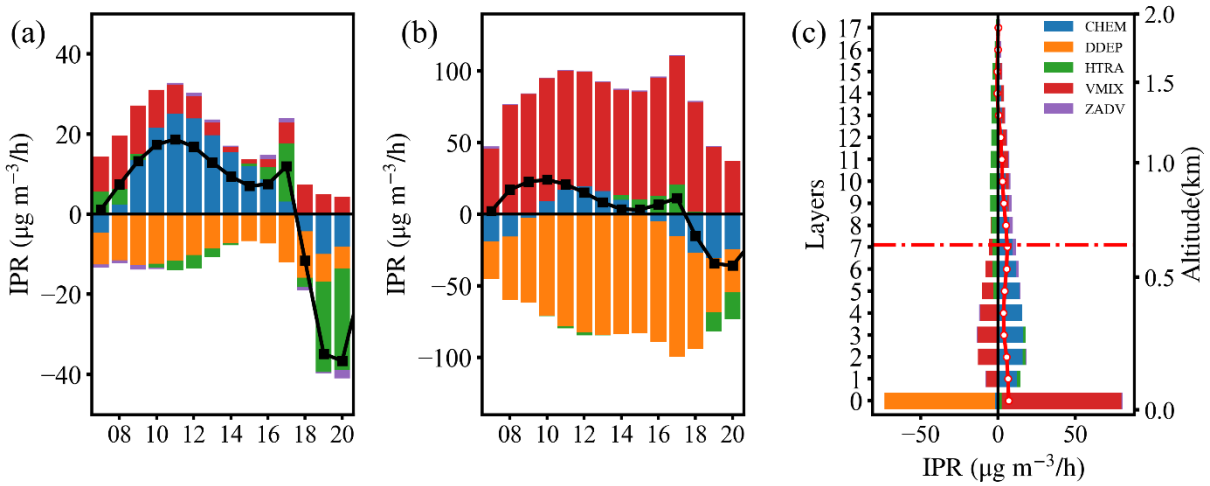


Figure S18. The average spatial distribution of contribution of ADRE (YFb-NoFb) to (a) SWR, (b)PBLH, (c)T2, (d) WS, (e) $PM_{2.5}$, (f) NO-3, and (g) O_3 during 5-8 April.



506

507 **Figure S19.** The contribution of (a) the average O_3 in the boundary layer, (b) near ground O_3 and (c) O_3 in the daytime

508 vertical direction under the noFb scenario in Nanjing on 8 April. CHEM, DDEP, HTRA, VMIX, and ZADV mean

509 photochemical process, dry deposition, horizontal transport, vertical mixing and advection process. The red dotted line in

510 Figure S18c is the average height of boundary layer in daytime

511

512